Available online at www.sciencedirect.com

SciVerse ScienceDirect

Ceramics International 39 (2013) 3511–3518

CERAMICS INTERNATIONAL

www.elsevier.com/locate/ceramint

Electrospinning of magnetical bismuth ferrite nanofibers with photocatalytic activity

Wei Wang[a,b], Nan Li[a], Yue Chi[a], Yanjuan Li[a], Wenfu Yan[c], Xiaotian Li[a,*], Changlu Shao[d]

[a]School of Material Science and Engineering, Key Laboratory of Automobile Materials of Ministry of Education, Jilin University, Changchun 130012, China
[b]School of Chemical and Material Engineering, Jilin Institute of Chemical Technology, Jilin 132022, China
[c]State Key Laboratory of Inorganic Synthesis and Preparative Chemistry, College of Chemistry, Jilin University, Changchun 130012, China
[d]Center for Advanced Optoelectronic Functional Materials Research, Key Laboratory of UV Light-Emitting Materials and Technology of Ministry of Education, Northeast Normal University, Changchun 130024, China

Received 10 September 2012; received in revised form 8 October 2012; accepted 9 October 2012
Available online 17 October 2012

Abstract

Bismuth ferrite ($BiFeO_3$) nanofibers were prepared by combining the electrospinning technique with sol–gel chemistry. The structural features of the as-prepared nanofibers were characterized by X-ray diffraction (XRD), scanning electron microscopy (SEM) and transmission electron microscopy (TEM). The obtained $BiFeO_3$ nanofibers showed a rhombohedral perovskite structure after getting annealed in an argon atmosphere. Both SEM and TEM results showed that $BiFeO_3$ fibers were composed of nanocrystalline particles. The photocatalytic behaviors of $BiFeO_3$ nanofibers were investigated by the degradation of Rhodamine B (RhB). $BiFeO_3$ nanofibers exhibited excellent catalytic activity under UV light irradiation, as well as under visible light irradiation in the presence of H_2O_2. The catalyst was further examined by magnetic measurement. The $BiFeO_3$ nanofibers exhibited a ferromagnetic behavior at room temperature, which was associated with the nanometer-size of $BiFeO_3$ particles. This provides an easy and efficient way to recover $BiFeO_3$ photocatalysts from the suspension system by applying an external magnetic field.

Keywords: C. Magnetic properties; $BiFeO_3$; Electrospinning; Photocatalyst

1. Introduction

With the rapid development of global industrialization, resource over-exploitation and environmental pollution problem are getting worse, which lead to severe damage of ecological balance. In recent years, photocatalytic oxidation with semiconducting materials is a proposed route for purification and remediation of polluted water and air [1–4]. Among various semiconducting oxide photocatalysts, titanium oxide (TiO_2) has been proven to be the most promising material due to its high photoreactivity, nontoxicity, strong oxidizing activity and long-term stability against photocorrosion and chemical corrosion [5,6]. However, owing to the large band-energy gap (3.2 eV for anatase), TiO_2 mainly absorbs UV light (which covers only 3–5% of the total solar spectrum). This practically eliminates the use of sunlight as an energy source for photocatalysis. For this reason, improving photocatalytic activity of TiO_2 by modification has become an extensive research topic among scientists in the past few years. Doped TiO_2 photocatalysts could be activated by visible light [7–9] but they always display poor activity and durability because of their limited amount and easy filtering of dopants. Moreover, introducing carbon-based materials with conjugated systems (such as carbon nanotubes, graphene, graphdiyne) into TiO_2 photocatalysts could also extend the adsorption wavelenth range and increase the photocatalytical activity [10–12]. Therefore, it is of great interest to develop efficient visible light responsive photocatalysts to extend absorption wavelength range into the visible light region, which accounts for more than half of the solar spectrum.

In semiconducting oxides, the conduction band levels of the small band-gap semiconductors are usually low due to the formation of the deep valence bands by O2p. This restricts

*Corresponding author. Tel.: +86 431 85168445; fax: +86 431 85168444.
E-mail address: xiaotianli@jlu.edu.cn (X. Li).

0272-8842/$ - see front matter © 2012 Elsevier Ltd and Techna Group S.r.l. All rights reserved.
http://dx.doi.org/10.1016/j.ceramint.2012.10.175

the development of visible-light-driven and stable oxide photocatalysts. From this viewpoint, it is necessary to control the valence band with orbitals of some elements instead of O2p. Bismuth is a potential candidate for such a valence band control element [13]. Bi-contained perovskite oxides often offer great optical properties for photocatalytic applications. Perovskite-type bismuth ferrite ($BiFeO_3$) has wide applications as photocatalytic materials owing to the small band-gap energy (~2.2 eV), and high chemical stability. Luo et al. have synthesized $SrTiO_3$-coated $BiFeO_3$ core/shell nanostructures, which have high photocatalytic efficiencies for H_2 production under visible light irradiation [14]. Li et al. have synthesized $BiFeO_3$ microcrystals, which exhibited excellent photocatalytic activity for the degradation of Congo red [15]. Furthermore, according to recent studies, photocatalytic properties of $BiFeO_3$ rely to a certain extent on the morphology of the sample. Two-dimensional $BiFeO_3$ plates showed a much higher photocatalytic activity than that of $BiFeO_3$ bulk materials for photodecoloration of orange II under visible light irradiation [16]. Li et al. also showed that, contrasted with $BiFeO_3$ microspheres and microcubes, $BiFeO_3$ submicrocubes exhibited better photocatalytic activity for the degradation of Congo Red under visible light illumination [15]. In addition, $BiFeO_3$ is one of the representative multiferroic materials, showing the coexistence of magnetic and ferroelectric orders over a certain range of temperature above room temperature. The perovskite-type $BiFeO_3$ exhibits a relatively high antiferromagnetic Neel temperature (T_N~370 °C) and ferroelectric Curie temperature (T_C~830 °C). Due to these excellent properties, $BiFeO_3$-based materials could provide some opportunities for potential applications in many fields, such as radio, television, microwave and satellite communication, bubble memory devices, audio video and digital recording [17–20]. $BiFeO_3$ nanomaterials have been prepared by using a variety of synthetic methods, such as conventional hydrothermal synthesis [21–24], polymer-assisted hydrothermal synthesis [25], microwave–hydrothermal synthesis [26], mineralizer-assisted hydrothermal synthesis [23], microwave-induced solid-state decomposition [27], sol–gel process [28–30], Pechini [31] and modified Pechini method [32], molten-salt method [33,34], sonochemical and microemulsion techniques [35], mechanochemical synthesis [36], co-precipitation [37–40], EDTA complexing sol–gel process [41], polymeric precursor method [42,43], ferrioxalate precursor method [44], combustion synthesis [45–47], polymer-directed solvothermal route [48], polyacrylamide gel route [49], tartaric acid-assisted gel strategy [50], and so forth. Among the various chemical methods, electrospinning is a straightforward, versatile, and efficient method to obtain the continuous polymer, polymer/inorganic hybrid, and inorganic nanofibers with diameters ranging from tens of nanometers to submicrometer and high surface-to-volume ratio [51,52].

In the present study, we report a successful attempt to fabricate $BiFeO_3$ nanofibers by combining sol–gel method with the electrospinning technique. The as-prepared nanofibers displayed high photocatalytic activity under UV light and visible light irradiation in a photochemical reactor. It is shown that the synthesized $BiFeO_3$ nanofibers exhibited good magnetic response with photocatalytic activity and this photocatalyst can be easily recovered by applying an external magnetic field while maintaining the photocatalytic activity.

2. Experimental

2.1. Catalysts preparation

All chemical reagents used in the present work were analytical grade and used as received without further purification. $BiFeO_3$ nanofibers were fabricated by an electrospinning method described as follows. 2 g of $Bi(NO_3)_3 \cdot 5\,H_2O$ and 1.5 g of $Fe(NO_3)_3 \cdot H_2O$ were dissolved in 5 mL of 2-methoxyethanol under mechanical stirring. Then 2.5 mL of glacial acetic acid and 0.025 mL of ethanolamine were added to adjust the viscosity and pH value of the solution under constant stirring. Polyvinyl pyrrolidone (PVP) with molecular weight 130,0000 was added to 11.25 mL of dimethyl formamide (DMF)/acetone (2:1 v/v) mixed solvent. The above two solutions were mixed and stirred continuously to form a homogenous 0.08 g/ml PVP solution. The obtained precursor solution was then loaded into a plastic syringe for the electrospinning. The needle tip of the syringe was connected to a high voltage that can generate a direct current (DC) voltage of 13 kV. An aluminum foil was employed as the collector attached to the cathode, and the distance between the needle tip and the collector was 10 cm. The solution jet was solidified by evaporation of solvent and a nonwoven fibrous mat was formed on the collector. The as-collected composite nanofibers were dried in an oven at 60 °C for 24 h, followed by heating at 350 °C for 30 min in air and thermal annealing at 550 °C for 2 h in argon atmosphere.

2.2. Characterization

The crystallization and phase formation of the resulting $BiFeO_3$ samples were studied with the Bruker D8 Advance X-ray diffractometer using CuK_α radiation at 40 kV and 100 mA. The morphology of the products was observed by a JEOL JSM-6700F field emission scanning electron microscope (FE-SEM) after being gold-coated. Transmission electron microscopy (TEM) experiments were performed on a JEOL JEM-2010 electron microscope. UV–vis diffuse reflectance spectroscopy of the sample was measured by a Bws003 spectrophotometer. The magnetic measurements were carried out on a MPM5-XL-5 superconductive quantum interference device (SQUID) magnetometer at ambient temperature (300 K).

2.3. Photocatalytic degradation experiments

The photocatalytic activities of the prepared products were evaluated through measuring the degradation of Rhodamine B (RhB) at room temperature. The photoreactor was designed with an internal light source (a 50 W high-pressure Hg lamp

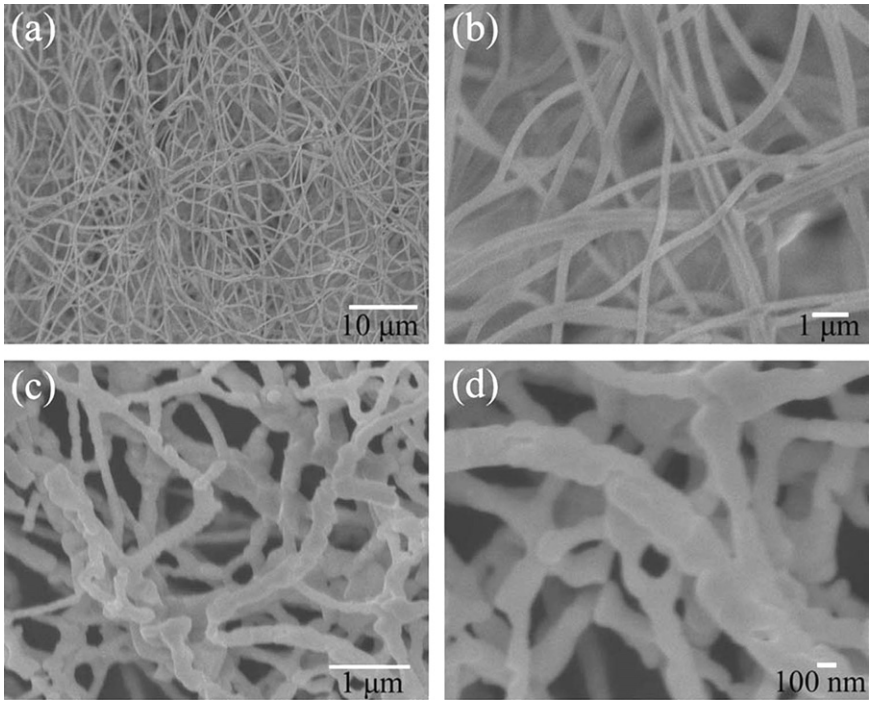

Fig. 1. SEM images of the as-spun PVP/inorganic composite fibers (a,b) and the annealed $BiFeO_3$ nanofibers (c,d).

with main emission wavelength of 313 nm was used as UV light source, and a 150 W high-pressure Xe lamp equipped with a cut-off glass filter transmitting $\lambda > 420$ nm was used as visible light source), which was surrounded by a water-cooling quartz jacket to cool the lamp. 10 mg of nanofibers were added to 100 mL RhB aqueous solution with a concentration of 10 mg/L to get a suspension. Prior to photooxidation, the suspension was stirred in the dark for 30 min to obtain a good dispersion and establish an adsorption–desorption equilibrium between the organic molecules and the catalyst surfaces. The adsorption of RhB on $BiFeO_3$ nanofibers was determined by the concentration difference between the original RhB solution and the filtrates of the RhB/$BiFeO_3$ suspensions. Decrease in the concentrations of dyes was recorded using a UV–visible spectrophotometer (UV-2500). For visible light irradiation, the degradation reaction was initiated by adding 0.1 mL H_2O_2 (30%). At certain intervals of illumination, the samples of the reaction solution were taken out and then centrifuged for analyzing.

3. Results and discussion

The general morphology of the $BiFeO_3$ nanofibers was studied with SEM. Fig. 1a and b shows the SEM images of the as-spun PVP/inorganic composite nanofibers, revealing that the diameter of the as-spun fibers is in the range of 220–480 nm, while their length can reach several micrometers. It is observed that these randomly oriented nanofibers have smooth and uniform surface due to the amorphous nature of the nanofibers. Fig. 1c and d shows the SEM images of $BiFeO_3$ nanofibers obtained by heat-treating the above as-spun composite nanofibers, which exhibit a little shrinkage with the diameter ranging from 100 to 370 nm, due to the decomposition of PVP. Furthermore, the length of $BiFeO_3$ nanofibers retains several micrometers. By carefully observing the surface of nanofibers, it can be found that the nanofibers appear to consist of linked particles, which is related to a dramatic change in crystal structure.

The crystalline structure of $BiFeO_3$ nanofibers was identified by XRD. Fig. 2 shows the XRD pattern of $BiFeO_3$ nanofibers fabricated by electrospinning. It is a challenge to prepare $BiFeO_3$ nanomaterials with high-purity, owing to the occurrence of impurity phase during sintering. By performing the heat treatment in a protective atmosphere, the formation of impurity phase would be restricted [53]. Therefore, in the present work, $BiFeO_3$ nanofibers were prepared by annealing in an argon atmosphere. The diffraction peaks in the XRD pattern correspond to the phase of $BiFeO_3$ with a rhombohedral perovskite structure belonging to R3c space group, which match well with the literature data (JCPDS 86-1518). This means that well-crystallized $BiFeO_3$ nanofibers could be obtained by the electrospinning technique followed by annealing in Ar.

A typical TEM image of $BiFeO_3$ nanofibers is shown in Fig. 3. The fibers are composed of dense nanocrystalline particles with an average size of about 90 nm, as shown in the inset of Fig. 3. From the results of SEM and TEM, it can be concluded that the fibers are composed of some nanopaticles.

It is known that the key factors in controlling a photocatalytic reaction include the optical absorption performance of semiconductors and the migration of the

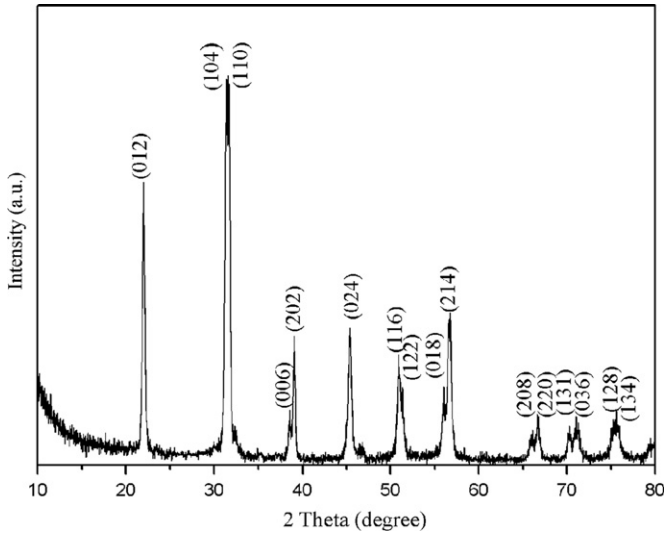

Fig. 2. XRD pattern of $BiFeO_3$ nanofibers prepared by electrospinning and subsequent heat-treatment.

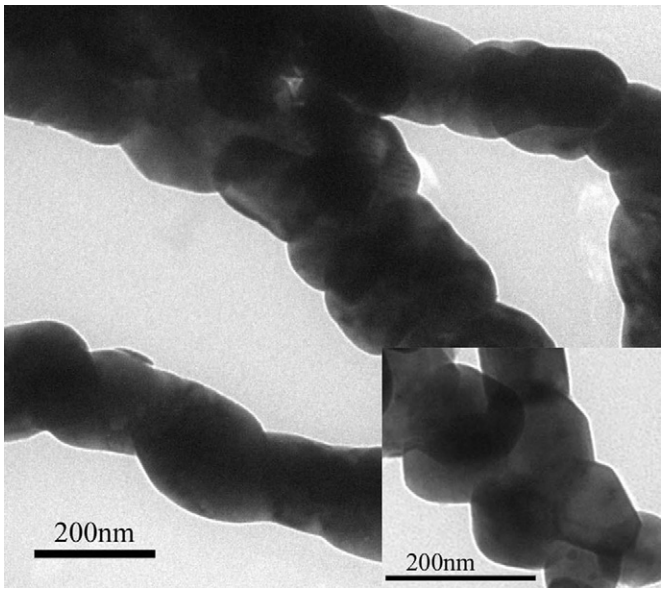

Fig. 3. TEM images of $BiFeO_3$ nanofibers. The inset is a local magnified TEM image of $BiFeO_3$ nanofibers.

light-induced electrons and holes, which are relevant to the electronic structure feature of the materials [54]. Fig. 4 shows the UV–vis diffuse reflectance spectrum of $BiFeO_3$ nanofibers. The absorption spectrum shows that $BiFeO_3$ products can absorb considerable amounts of visible light, indicating that $BiFeO_3$ nanofibers prepared by this method could be a kind of visible-light-driven photocatalytic material. The steep shape of the spectrum indicated that the visible light absorption was due to the electronic transition from the valence band to conduction band ($O^{2-}2p \rightarrow Fe^{3+}3d$) in $BiFeO_3$ lattice. The optical absorption coefficient near the band edge follows the equation [55] $\alpha hv = A(hv - Eg)^{n/2}$, where α, h, v, Eg, and A are absorption coefficient, Planck constant, light frequency, band-gap, and a constant, respectively. The corresponding energy band-gap

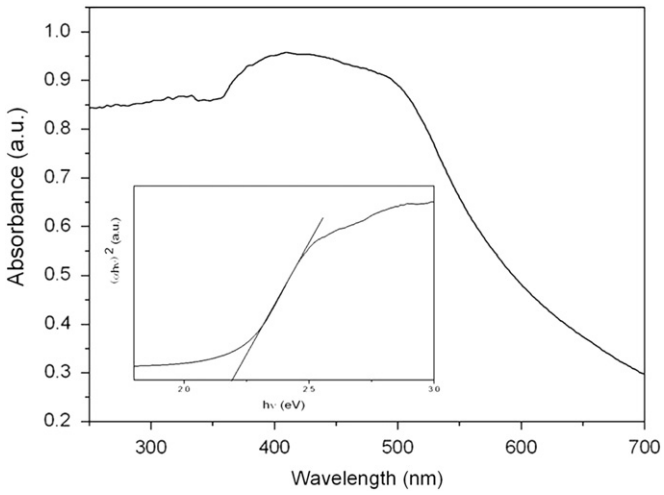

Fig. 4. UV–vis diffuse reflectance spectrum of $BiFeO_3$ nanofibers. The inset shows the corresponding $(\alpha hv)^2$–hv plot.

of $BiFeO_3$ photocatalyst can be obtained from the plot of $(\alpha hv)^2$ versus hv by extrapolating the straight portion of $(\alpha hv)^2$ to zero, as shown in the inset of Fig. 4. After calculation, the value is determined to be 2.19 eV for $BiFeO_3$ nanofibers, which is consistent with previous reports [56,24]. Such narrow band-gap is beneficial for the efficient utilization of visible light for photocatalysis.

To explore the photocatalytic activity of the $BiFeO_3$ fibers for the degradation of organic pollutants, the degradation of RhB in aqueous solution was tested. RhB was selected as the model pollutant because of its obvious absorption at 553 nm. Fig. 5a displays the temporal evolution of the spectral changes taking place during the photodegradation of RhB catalyzed by $BiFeO_3$ nanofibers under UV light irradiation. The rapid decrease of RhB absorption at the wavelength of 553 nm demonstrated the decomposition of RhB. After 80 min, the absorption peak disappeared, suggesting the complete decomposition of RhB. At the same time, the color of the suspension changes gradually, suggesting that the chromophoric structure of the RhB was decomposed. In the inset of Fig. 5a, the photocatalytic control experiments were performed in the presence of $BiFeO_3$ nanofibers but in the dark. It was showed that the decolorization of RhB solutions was not controlled by the surface adsorption but by the photodegradation of $BiFeO_3$ nanofibers. Besides, Fig. 5c and d shows the degradation curves of RhB over $BiFeO_3$ nanofibers under visible light irradiation. As shown in Fig. 5d, RhB is hardly degraded in the absence of either $BiFeO_3$ nanofibers or H_2O_2. The degradation rate of RhB was 14.3% after 5 h of visible light illumination in the presence of $BiFeO_3$ nanofibers. But the degradation efficiency of RhB was significantly promoted in the system of the simultaneous presence of $BiFeO_3$ nanofibers and H_2O_2 at pH 5.0. After 5 h, about 97.3% of RhB was degraded under visible light irradiation. During such process, H_2O_2 molecules are absorbed on the surface of $BiFeO_3$ nanofibers, and the adsorbed H_2O_2 molecules are catalytically activated by $BiFeO_3$ nanofibers to generate •OH radicals, which then break down RhB into smaller organic molecules

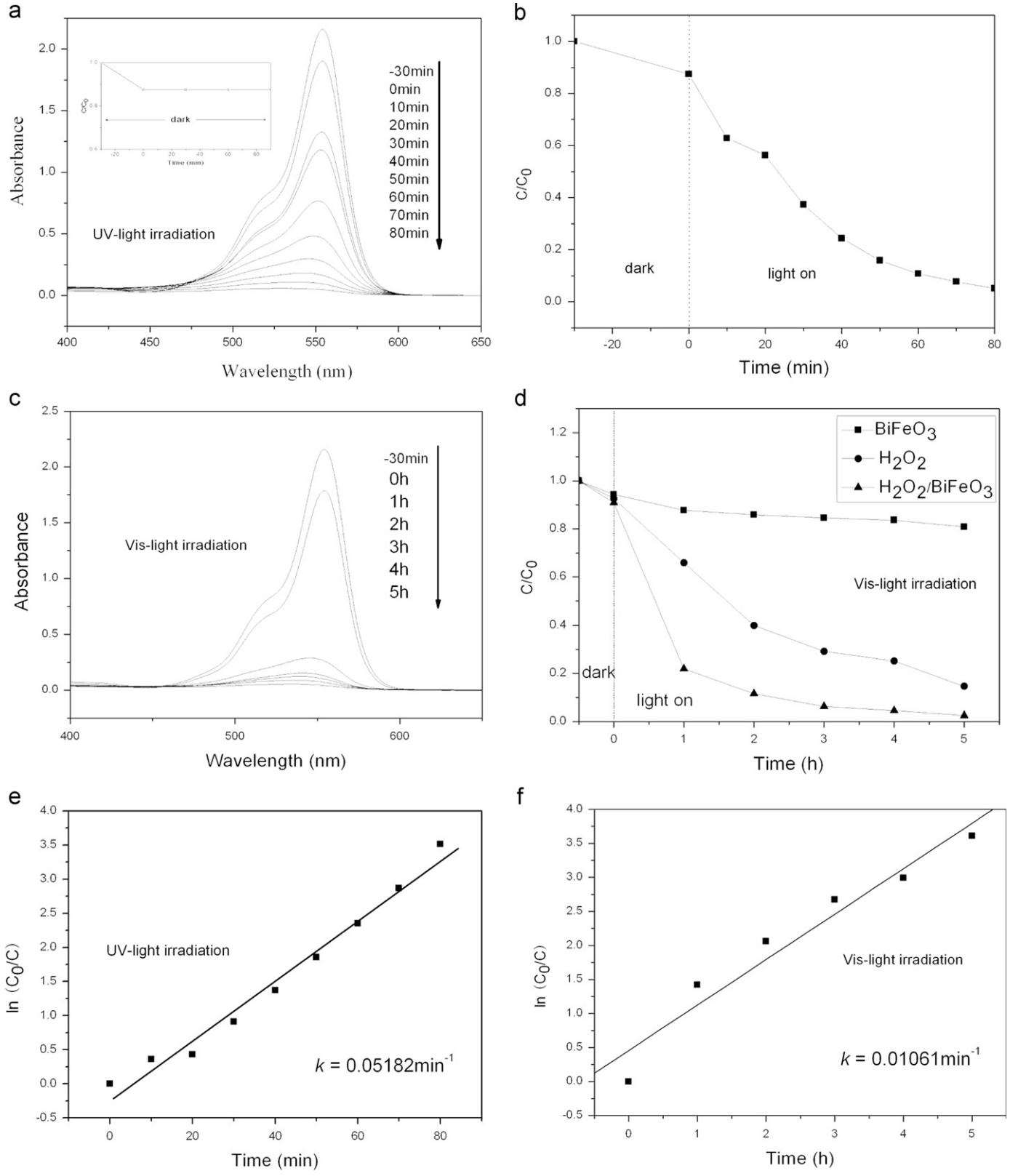

Fig. 5. (a,b) Absorption spectra and photocatalytic degradations of RhB solution in the presence of $BiFeO_3$ nanofibers under UV light irradiation. The inset was the degradation profile of RhB solutions in the presence of $BiFeO_3$ nanofibers but in the dark; (c,d) absorption spectra and photocatalytic degradations of RhB solution in the presence of $H_2O_2/BiFeO_3$ nanofibers under visible light irradiation. The degradations in $BiFeO_3$ nanofibers and H_2O_2 catalyst were presented for comparison; (e,f) kinetic linear simulation curves of photocatalytic degradation of RhB under UV and visible light irradiation. $BiFeO_3$ nanofibers and $H_2O_2/BiFeO_3$ nanofibers were used as catalyst.

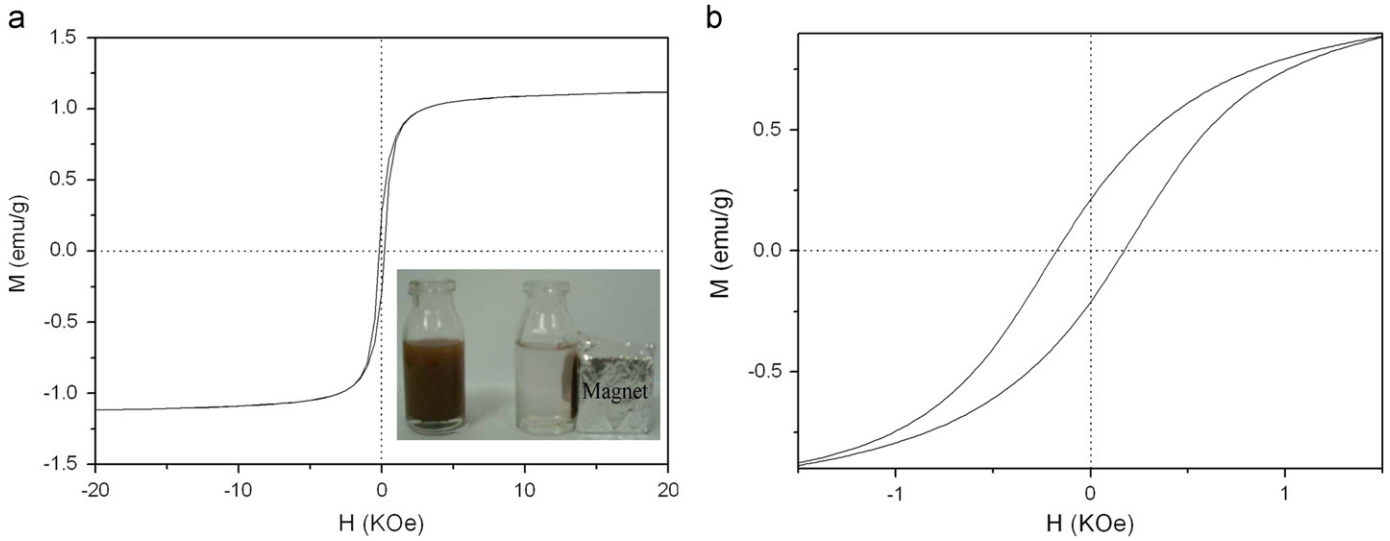

Fig. 6. (a) Magnetization curve of $BiFeO_3$ nanofibers at room temperature (the inset is the magnetic separation of $BiFeO_3$ nanofibers under an external magnet); (b) partially enlarged image of curve (a).

and CO_2 [57]. The kinetic linear simulation curves of the photocatalytic degradation of RhB by $BiFeO_3$ nanofibers were presented in Fig. 5e and f. The results show that the above degradation reactions tend to follow a Langmuir–Hinshelwood apparent first-order kinetics model ($\ln C_0/C = kt$) in the present work because of the low initial concentrations of the reactants (10 mg/L for RhB in the present experiment) [58,59]. The apparent first-order rate constant k for $BiFeO_3$ photocatalysts calculated from the above formula was shown in Fig. 5e and f.

A proposed mechanism for the photocatalytic behavior of the $BiFeO_3$ nanofibers was described as follows: $BiFeO_3$ has a rhombohedral perovskite structure at room temperature. During the synthesis process, it is easy for the mole ratio of Bi/Fe to deviate from chemical stoichiometric proportion, owing to the partial bismuth volatilization. Thus, they lost the metal atoms at the crank points of the crystal lattice and result in metal vacancies. In order to keep the charge balance, oxygen vacancies should be formed which lead to the increase of oxygen absorbed. Therefore, the concentration of reactive OH• becomes higher when oxygen absorbed increased, which helps in the photocatalytic reaction [60].

The magnetic property of $BiFeO_3$ nanofibers is very important for practical applications. Fig. 6a shows the magnetic hysteresis loop of $BiFeO_3$ nanofibers measured at room temperature, while Fig. 6b is an amplified view of the curve. The hysteresis loop of $BiFeO_3$ nanofibers presented a small hysteresis loop, which suggests the samples have a ferromagnetic behavior with saturation magnetization (Ms), remnant magnetization (Mr), and coercivity (Hc) of 4.4 emu/g, 0.83 emu/g, and 170 Oe, respectively. Different from the linear M versus H relationship commonly displayed by bulk crystalline $BiFeO_3$ [61], $BiFeO_3$ nanofibers exhibit nonlinearity in M versus H curve. The bulk $BiFeO_3$ exhibits a disproportionate spiral spin structure that cancels the macroscopic magnetization. At the same time, it is observed that coercivity is commonly not present in bulk $BiFeO_3$. Consequently, the nonlinear hysteresis curve of fibers is associated with the nanometer-size of $BiFeO_3$ particles. The magnetic separation ability of $BiFeO_3$ nanofibers was tested by placing a magnet near the glass bottle. When a magnet was placed outside the glass bottle, the samples were attracted to the magnet side within a short period (inset of Fig. 6a). When the magnet was taken away, $BiFeO_3$ nanofibers are well dispersed again by shaking. Therefore, this will provide an easy and efficient way to separate $BiFeO_3$ photocatalysts from the suspension system under an external magnetic field.

4. Conclusions

In summary, $BiFeO_3$ nanofibers were successfully fabricated via facile electrospinning technique combining with sol–gel method. These fibers possessed a rhombohedral distorted perovskite structure, which was obtained after getting annealed in argon atmosphere. $BiFeO_3$ nanofibers prepared through this method are of high photocatalytic activity under UV and visible light irradiation. When exposed to visible light, a removal of 97.3% for RhB was observed. Meanwhile, $BiFeO_3$ nanofibers exhibit a ferromagnetic behavior at room temperature with 170 Oe coercivity and 4.4 emu/g saturation magnetization, which is associated with the nanometer-size of $BiFeO_3$ particles. Thus, the obtained $BiFeO_3$ nanofibers with high photocatalytic activity are very useful for cleaning wastewater with the help of magnetic separation. This study provided a possible treatment approach for organic pollutants by using visible light in aqueous ecosystems.

Acknowledgments

This work was supported financially by the National Natural Science Foundation of China (nos. 21076094 and 20743005).

References

[1] M.R. Hoffmann, S.T. Martin, W.Y. Choi, D.W. Bahnemann, Environmental applications of semiconductor photocatalysis, Chemical Review 95 (1995) 69–96.

[2] J. Yu, J.C. Yu, M.K.P. Leung, W. Ho, Effects of acidic and basic hydrolysis catalysts on the photocatalytic activity and microstructures of bimodal mesoporous titania, Journal of Catalysis 217 (2003) 69–78.

[3] X. Wang, W. Lian, X. Fu, J.M. Basset, F. Lefebvre, Structure, preparation and photocatalytic activity of titanium oxides on MCM-41 surface, Journal of Catalysis 238 (2006) 13–20.

[4] C. Zhang, Y.F. Zhu, Synthesis of square Bi_2WO_6 nanoplates as high-activity visible-light-driven photocatalysts, Chemistry of Materials 17 (2005) 3537–3545.

[5] L. Cesar, A. Kay, J.A.G. Martinez, M.J. Gratzel, Translucent thin film Fe_2O_3 photoanodes for efficient water splitting by sunlight: nanostructure-directing effect of Si-doping, Journal of the American Chemical Society 128 (2006) 4582–4583.

[6] S.F. Chen, G.Y. Cao, The preparation of nitrogen-doped photocatalyst $TiO_{2-X}N_X$ by ball milling, Chemical Physics Letters 413 (2005) 404–409.

[7] W.Y. Choi, A. Termin, M.R. Hoffmann, The role of metal ion dopants in quantum-sized TiO_2: correlation between photoreactivity and charge carrier recombination dynamics, The Journal of Physical Chemistry 98 (1994) 13669–13679.

[8] M. Sathish, B. Viswanathan, R.P. Viswanath, C.S. Gopinath, Synthesis, characterization, electronic structure, and photocatalytic activity of nitrogen-doped TiO_2 nanocatalyst, Chemistry of Materials 17 (2005) 6349–6353.

[9] D. Li, H. Haneda, N.K. Labhsetwar, S. Hishita, N. Ohashi, Visible-light-driven photocatalysis on fluorine-doped TiO_2 powders by the creation of surface oxygen vacancies, Chemical Physics Letters 401 (2005) 579–584.

[10] H. Zhang, Xiaojun Lv, Yueming Li, Y. Wang, Jinghong Li, P25-graphene composite as a high performance photocatalyst, ACS Nano 4 (2010) 380–386.

[11] J. Du, X.Y. Lai, N.L. Yang, J. Zhai, D. Kisailus, F.B. Su, D. Wang, L. Jiang, Hierarchically ordered macro-mesoporous TiO_2 graphene composite films: improved mass transfer, reduced charge recombination, and their enhanced photocatalytic activities, ACS Nano 5 (2011) 590–596.

[12] S. Wang, L.X. Yi, J.E. Halpert, X.Y. Lai, Y.Y. Liu, H.B. Cao, R.B. Yu, D. Wang, Y.L. Li, A novel and highly efficient photocatalyst based on P25–graphdiyne nanocomposite, Small 8 (2012) 265–271.

[13] H.B. Fu, C.S. Pan, W.Q. Yao, Y.F. Zhu, Visible-light-induced degradation of Rhodamine B by nanosized Bi_2WO_6, The Journal of Physical Chemistry B 109 (2005) 22432–22439.

[14] J.H. Luo, P.A. Maggard, Hydrothermal synthesis and photocatalytic activities of $SrTiO_3$-coated Fe_2O_3 and $BiFeO_3$, Advanced Materials 18 (2006) 514–517.

[15] S. Li, Y.H. Lin, B.P. Zhang, Y. Wang, C.W. Nan, Controlled fabrication of $BiFeO_3$ uniform microcrystals and their magnetic and photocatalytic behaviors, Journal of Physical Chemistry C 114 (2010) 2903–2908.

[16] X.M. Lu, J.M. Xie, Y.Z. Song, J.M. Lin, Surfactant-assisted hydrothermal preparation of submicrometer-sized two-dimensional $BiFeO_3$ plates and their photocatalytic activity, Journal of Materials Science 42 (2007) 6824–6827.

[17] J.D. Bucci, B.K. Robertson, W.J. James, The precision determination of the lattice parameters and the coefficients of thermal expansion of $BiFeO_3$, Journal of Applied Crystallography 5 (1972) 187–191.

[18] F. Kubel, H. Schmid, Structure of a ferroelectric and ferroelastic monodomain crystal of the perovskite $BiFeO_3$, Acta crystallographica B 46 (1990) 698–702.

[19] V.R. Palkar, R. Pinto, $BiFeO_3$ thin films: novel effects, **Pramana—Journal of Physics** 58 (2002) 1003–1008.

[20] Y.P. Wang, L. Zohu, M.F. Zhang, X.Y. Chen, J.M. Liu, Z.G. Liu, Room-temperature saturated ferroelectric polarization in $BiFeO_3$ ceramics synthesized by rapid liquid-phase sintering, Applied Physics Letters 84 (2004) 1731–1733.

[21] C. Chen, J.R. Cheng, S.W. Yu, L.J. Che, Z.Y. Meng, Hydrothermal synthesis of perovskite bismuth ferrite crystallites, Journal of Crystal Growth 291 (2006) 135–139.

[22] S. Basu, M. Pal, D. Chakravorty, Magnetic properties of hydrothermally synthesized $BiFeO_3$ nanoparticles, Journal of Magnetism and Magnetic Materials 320 (2008) 3361–3365.

[23] Y.G. Wang, G. Xu, Z.H. Ren, X. Wei, W.J. Weng, P.Y. Du, G. Shen, G.R. Han, Mineralizer-assisted hydrothermal synthesis and characterization of $BiFeO_3$ nanoparticles, Journal of the American Ceramic Society 90 (2007) 2615–2617.

[24] C.M. Cho, J.H. Noh, I.-S. Cho, J.-S. An, K.S. Hong, Low-temperature hydrothermal synthesis of pure $BiFeO_3$ nanopowders using triethanolamine and their applications as visible-light photocatalysts, Journal of the American Ceramic Society 91 (2008) 3753–3755.

[25] Y.G. Wang, G. Xu, Z.H. Ren, X. Wei, W.J. Weng, P.Y. Du, G. Shen, G.R. Han, Low temperature polymer assisted hydrothermal synthesis of bismuth ferrite nanoparticles, Ceramics International 34 (2008) 1569–1571.

[26] J. Prado-Gonjal, M.E. Villafuerte-Castrejón, L. Fuentes, E. Morán, Microwave–hydrothermal synthesis of the multiferroic $BiFeO_3$, Materials Research Bulletin 44 (2009) 1734–1737.

[27] S. Farhadi, N. Rashidi, Microwave-induced solid-state decomposition of the $Bi[Fe(CN)_6]\cdot 5H_2O$ precursor: a novel route for the rapid and facile synthesis of pure and single-phase $BiFeO_3$ nanopowder, Journal of Alloys and Compounds 503 (2010) 439–444.

[28] M. Kumar, K.I. Yadav, G.D. Varma, Large magnetization and weak polarization in sol–gel derived $BiFeO_3$ ceramics, Materials Letters 62 (2008) 1159–1161.

[29] J.H. Xu, H. Ke, D.C. Jia, W. Wang, Y. Zhou, Low-temperature synthesis of $BiFeO_3$ nanopowders via a sol–gel method, Journal of Alloys and Compounds 472 (2009) 473–477.

[30] T.J. Park, G.C. Papaefthymiou, A.J. Viescas, A.R. Moodenbaugh, S.S. Wong, Size-dependent magnetic properties of single-crystalline multiferroic $BiFeO_3$ Nanoparticles, Nano Letters 7 (2007) 766–772.

[31] E.A.V. Ferri, I.A. Santos, E. Radovanovic, R. Bonzanini, E.M. Girotto, Chemical characterization of $BiFeO_3$ obtained by Pechini method, Journal of the Brazilian Chemical Society 19 (2008) 1153–1157.

[32] S.M. Selbach, T. Tybell, M.A. Einarsrud, T. Grande, Size-dependent properties of multiferroic $BiFeO_3$ nanoparticles, Chemistry of Materials 19 (2007) 6478–6484.

[33] J. Chen, X.R. Xing, A. Watson, W. Wang, R.B. Yu, J.X. Deng, L. Yan, C. Sun, X.B. Chen, Rapid synthesis of multiferroic $BiFeO_3$ single-crystalline nanostructures, Chemistry of Materials 19 (2007) 3598–3600.

[34] X.B. He, L. Gao, Synthesis of pure phase $BiFeO_3$ powders in molten alkali metal nitrates, Ceramics International 35 (2009) 975–978.

[35] N. Das, R. Majumdar, A. Sen, H.S. Maiti, Nanosized bismuth ferrite powder prepared through sonochemical and microemulsion techniques, Materials Letters 61 (2007) 2100–2104.

[36] I. Szafraniak, M. Polomska, B. Hilczer, A. Pietraszko, L. Kepinski, Characterization of $BiFeO_3$ nanopowder obtained by mechanochemical synthesis, Journal of the European Ceramic Society 27 (2007) 4399–4402.

[37] H. Ke, W. Wang, Y.B. Wang, J.H. Xu, D.C. Jia, Z. Lu, Y. Zhou, Factors controlling pure-phase multiferroic $BiFeO_3$ powders synthesized by chemical co-precipitation, Journal of Alloys and Compounds 509 (2011) 2192–2197.

[38] H.Y. Bo, G.Q. Tan, H.Y. Miao, A. Xia, Co-precipitation synthesis of $BiFeO_3$ powders, Advances in Materials Research 105–106 (2010) 286–288.

[39] Z.K. Liu, Y.J. Qi, C.J. Lu, High efficient ultraviolet photocatalytic activity of $BiFeO_3$ nanoparticles synthesized by a chemical coprecipitation process, Journal of Materials Science 21 (2010) 380–384.

[40] V.R. Palkar, D.C. Kundaliya, S.K. Malik, Effect of Mn substitution on magnetoelectric properties of bismuth ferrite system, Journal of Applied Physics 93 (2003) 4337–4339.

[41] J. Wei, D.S. Xue, Low-temperature synthesis of $BiFeO_3$ nanoparticles by ethylenediaminetetraacetic acid complexing sol–gel process, Materials Research Bulletin 43 (2008) 3368–3373.
[42] M. Popa, D. Crespo, J.M. Calderon-Moreno, S. Preda, V. Fruth, Synthesis and structural characterization of single-phase $BiFeO_3$ powders from a polymeric precursor, Journal of the American Ceramic Society 90 (2007) 2723–2727.
[43] S.M. Selbach, M.A. Einarsrud, T. Tybell, T. Grande, Low-loss microwave dielectrics in the $(Mg_{1-x}Zn_x)_2TiO_4$ ceramics, Journal of the American Ceramic Society 90 (2007) 3430–3434.
[44] S. Ghosh, S. Dasgupta, A. Sen, H.S. Maiti, Low temperature synthesis of bismuth ferrite nanoparticles by a ferrioxalate precursor method, Materials Research Bulletin 40 (2005) 2073–2079.
[45] V. Fruth, D. Berger, C. Matei, A. Ianculescu, M. Popa, E. Tenea, M. Zaharescu, Preparation and characterization of $BiFeO_3$ nanopowders, Journal De Physique Iv 128 (2005) 7–11.
[46] V. Fruth, L. Mitoseriu, D. Berger, A. Ianculescu, C. Matei, S. Preda, M. Zaharescu, Preparation and characterization of $BiFeO_3$ ceramic, Progress in Solid State Chemistry 35 (2007) 193–202.
[47] S. Farhadi, M. Zaidi, Bismuth ferrite ($BiFeO_3$) nanopowder prepared by sucrose-assisted combustion method: a novel and reusable heterogeneous catalyst for acetylation of amines, alcohols and phenols under solvent-free conditions, Journal of Molecular Catalysis A: Chemical 299 (2009) 18–25.
[48] L. Zhang, X.F. Cao, Y.L. Ma, X.T. Chen, Z.L. Xue, Polymer-directed synthesis and magnetic property of nanoparticles-assembled $BiFeO_3$ microrods, Journal of Solid State Chemistry 183 (2010) 1761–1766.
[49] T. Xian, H. Yang, X. Shen, J.L. Jiang, Z.Q. Wei, W.J. Feng, Preparation of high-quality $BiFeO_3$ nanopowders via a polyacrylamide gel route, Journal of Alloys and Compounds 480 (2009) 889–892.
[50] X. Wang, Y.G. Zhang, Z.B. Wu, Magnetic and optical properties of multiferroic bismuth ferrite nanoparticles by tartaric acid-assisted sol–gel strategy, Materials Letters 64 (2010) 486–488.
[51] J.Y. Park, I.H. Lee, G.N. Bea, Optimization of the electrospinning conditions for preparation of nanofibers from polyvinylacetate (PVAc) in ethanol solvent, Journal of Industrial and Engineering Chemistry 14 (2008) 707–713.
[52] J.Y. Park, I.H. Lee, Relative humidity effect on the preparation of porous electrospun polystyrene fibers, Journal of Nanoscience and Nanotechnology 10 (2010) 3473–3477.
[53] C. Ternon, J. Therya, T. Barona, C. Ducrosb, F. Sanchetteb, J. Kreiselc, Structural properties of films grown by magnetron sputtering of a $BiFeO_3$ target, Thin Solid Films 515 (2006) 481–484.
[54] J. Tang, Z. Zou, J. Ye, Effects of substituting Sr^{2+} and Ba^{2+} for Ca^{2+} on the structural properties and photocatalytic behaviors of $CaIn_2O_4$, Chemistry of Materials 16 (2004) 1644–1649.
[55] M.A. Butler, Photoelectrolysis and physical properties of the semiconducting electrode WO_2, Journal of Applied Physics 48 (1977) 1914–1920.
[56] F. Gao, X. Chen, K. Yin, S. Dong, Z. Ren, F. Yuan, T. Yu, Z. Zou, J.-M. Liu, Visible-light photocatalytic properties of weak magnetic $BiFeO_3$ nanoparticles, Advanced Materials 19 (2007) 2889–2892.
[57] W. Luo, L.H. Zhu, N. Wang, H.Q. Tang, M.J. Cao, Y.B. She, Efficient removal of organic pollutants with magnetic nanoscaled $BiFeO_3$ as a reusable heterogeneous fenton-like catalyst, Environmental Science and Technology 44 (2010) 1786–1791.
[58] C.S. Turchi, D.F. Ollis, Photocatalytic degradation of organic water contaminants: mechanisms involving hydroxyl radical attack, Journal of Catalysis 122 (1990) 178–192.
[59] M.S. Lee, S.S. Park, G.D. Lee, C.S. Ju, S.S. Hong, Synthesis of TiO_2 particles by reverse microemulsion method using nonionic surfactants with different hydrophilic and hydrophobic group and their photocatalytic activity, Catalysis Today 101 (2005) 283–290.
[60] X.S. Niu, H.H. Li, G.G. Liu, Preparation, characterization and photocatalytic properties of $REFeO_3$ (RE=Sm, Eu, Gd), Journal of Molecular Catalysis A: Chemical 232 (2005) 89–93.
[61] J. Wang, J.B. Neaton, H. Zheng, V. Nagarajan, S.B. Ogale, B. Liu, D. Viehland, V. Vaithyanathan, D.G. Schlom, U.V. Waghmare, N.A. Spaldin, K.M. Rabe, M. Wuttig, R. Ramesh, Epitaxial $BiFeO_3$ multiferroic thin film heterostructures, Science 299 (2003) 1719–1722.